A network of coiled-coil and actin-like proteins controls the cellular organization of magnetosome organelles in deep-branching magnetotactic bacteria

Virginia V. Russell[1], Anthony T. Iavarone[2], Ertan Ozyamak[1,3], Carly Grant[1,4] and Arash Komeili[1]

[1] Plant and Microbiology, University of California Berkeley, Berkeley, California, USA.
[2] QB3/Chemistry Mass Spectrometry Facility, University of California Berkeley, Berkeley, California, USA.
[3] Current affiliation: Bio-Rad Laboratories, Hercules, California, USA
[4] Current affiliation: Entrepreneurship Program, UCSF Rosenman Institute, San Francisco, California, USA

Abstract

Magnetotactic Bacteria (MTB) are a diverse group of microorganisms that use magnetosomes, organelles composed of magnetite or greigite, to navigate along geomagnetic fields. While MTB span several phyla and exhibit diverse phenotypes, magnetosome formation has been mechanistically studied in only two species of *Alphaproteobacteria*. Here, we use *Desulfovibrio magneticus* RS-1 to uncover the mechanisms behind tooth-shaped magnetosome assembly in deep-branching MTB. Our findings show that magnetic particles in RS-1 initially form randomly within the cell before localizing to the positive cell curvature. Genetic and proteomic analyses indicate that early biomineralization involves membrane-associated proteins found in all MTB, while later stages depend on coiled-coil (Mad20, 23, 25, and 26) and actin-like (MamK and Mad28) proteins, most of which are unique to deep-branching MTB. These findings suggest that while biomineralization originates from a common ancestor, magnetosome chain organization has distinct evolutionarily origins among different MTB lineages.

Introduction

Magnetotactic Bacteria (MTB) are a diverse group of microorganisms that navigate along geomagnetic fields to locate low-oxygen environments in a process termed magneto-aerotaxis. This ability relies on magnetosomes—specialized organelles containing magnetic crystals of magnetite (Fe_3O_4) or greigite (Fe_3S_4) 50-70 nm in diameter, enclosed by a lipid bilayer membrane with a unique set of proteins[1,2]. Depending on the species, magnetosomes form single or multiple chains, that allow for alignment with external fields[3]. These features have made MTB models for studying bacterial organelle formation, biomineralization, and the global

35 geochemical cycling of iron[4]. MTB have also been deployed as potential vehicles for a variety of
36 biotechnological applications[5]. A key bottleneck in the study of MTB has been the limited
37 number of model organisms that sufficiently represent the mechanistic diversity and evolution of
38 magnetosome formation.

39 MTB are a polyphyletic group of microorganisms that belong to *Alphaproteobacteria*,
40 *Gammaproteobacteria*, *Candidatus Etaproteobacteria* classes in the *Pseudomonadota* phylum,
41 and the phyla *Desulfobacterota*, *Nitrospirota, Candidatus Omnitrophota*, and *Elusimicrobiota*
42 (Figure 1B). Metagenomic studies suggest MTB may also exist in the *Latescibacteria*,
43 *Planctomycetes*, *Nitrospinota*, *Fibrobacterota*, *Riflebacteria*, *Hydrogendentota*, *Myxococcota*,
44 *Bdellovibrionota* phyla and possibly more[2,6]. MTB exhibit diverse phenotypes, including
45 variations in crystal shape, chain organization, and magnetosome composition[3]. Phylogeny
46 correlates with some of these features; for instance, *Alphaproteobacteria* produce
47 cubooctahedral and prismatic magnetite crystals, while *Desulfobacterota* and other deep-
48 branching MTB (*Nitrospirota*, *Omnitrophota*, *Elusimicrobiota*) form irregular tooth-shaped
49 magnetite crystals thought to represent the ancestral magnetosome form (Figure 1C)[3].

50 Despite the vast diversity of MTB, most mechanistic studies have focused on two
51 Alphaproteobacterial species, *Magnetospirillum magneticum* AMB-1 and *Magnetospirillum*
52 *gryphiswaldense* MSR-1, which contain a conserved magnetosome gene cluster (MGC). The
53 MGC spans ~100 kilobases and includes 50-100 genes, with 29 necessary and sufficient for
54 magnetosome formation[7]. Depending on the accounting, only 5-9 core genes (*mamA*, *B*, *E*, I, K,
55 M, O, P and *Q*) are shared across all MTB[8,9]. However, many genes critical for magnetosome
56 formation in *Alphaproteobacteria* are absent in other MTB. In turn, group-specific genes are
57 found in the MGCs of other MTB. For instance, *mad* genes, originally named for '**m**agnetosome-
58 **a**ssociated ***D****eltaproteobacteria*,' are present in all deep-branching MTB. Similarly, *man*
59 (**m**agnetosome-**a**ssociated **N**itrospirota) genes are found in *Nitrospirota*, and *mae*
60 (**ma**gnetosome **E**lusimicrobiota) genes are found in *Elusimicrobiota*[8]. Since few non-
61 Alphaproteobacterial MTB are cultured, and most lack genetic systems, mechanisms of *mad*
62 gene function and irregular tooth-shaped magnetosome formation have remained elusive. This
63 is a critical barrier in the study of MTB as tooth-shaped magnetosomes are common in nature[3],
64 yet their biomineralization mechanisms remain unknown.

65 The most promising model for deep-branching MTB is *Desulfovibrio magneticus* RS-1, a
66 sulfate-reducing obligate anaerobe from the *Desulfobacterota* phylum (originally grouped within
67 *Deltaproteobacteria*) [10,11]. RS-1 synthesizes a single chain of irregular tooth-shaped magnetite
68 magnetosomes, organized into subchains of contiguous crystals separated by gaps along the

positive cell curvature (Figure 2C-*ii* and 2G). It is one of the few cultured non-Alphaproteobacterial MTB with a sequenced genome and the only deep-branching strain with tools for heterologous gene expression and genome editing[12–14]. Previous studies of RS-1 have highlighted several features distinguishing it from Alphaproteobacterial models. First, RS-1 produces tooth-shaped crystals. Second, unlike *Alphaproteobacteria*, mature RS-1 crystals appear to lack a lipid membrane[15], though its MGC contains proteins with predicted transmembrane domains, many of which are homologs of well-studied Mam proteins. Genetic studies show mutations in these genes disrupt magnetite formation, implying the involvement of a magnetosome membrane at some stage[12]. Finally, RS-1, like all deep-branching MTB, contains a suite of *mad* genes. One conspicuous feature of many Mad proteins is that they are predicted to contain one or multiple coiled-coil segments. These domains typically mediate homo- and hetero-polymeric interactions allowing for assembly of simple dimers to complex multimeric structures. In bacteria, proteins with coiled-coil domains are involved in organization and segregation of chromosomes, assembly and function of the type III secretion system, and formation of intermediate-like filaments that influence cell shape[16–19]. Bioinformatic analyses of deep-branching MTB have proposed roles in biomineralization, protein sorting, and chain organization for coiled-coil-domain containing Mad proteins[9]. However, direct experimental evidence of their function has remained mysterious.

Here, we comprehensively characterize the RS-1 biomineralization process to develop a deeper understanding of the mechanisms and evolution of magnetosome formation in deep-branching MTB. Using a conditional biomineralization assay combined with genetics and proteomics, we define specific steps in magnetic particle growth and identify specific factors associated with the progression of biomineralization and magnetosome chain formation. We find that early steps of biomineralization utilize proteins enriched in transmembrane domains including some encoded by *mam* genes common to all MTB. In contrast, localization, organization, and positioning of the magnetosome chain rely on the suite of coiled-coil domain-containing Mad proteins as well as the actin-like proteins, MamK and Mad28. These findings indicate a complex evolutionary history where iron biomineralization is an ancestral feature of all MTB while chain formation follows an independent and group-specific path.

Results

Hydrogen inhibition of magnetosome synthesis

102 Our first goal was to develop a robust system to visualize the steps of magnetosome
103 formation in RS-1. In other MTB, magnetite is not formed under iron-limiting conditions. Addition
104 of iron then triggers synchronized magnetosome chain development[20]. However, transitioning
105 from iron-limited to iron-replete conditions in RS-1 leads to the accumulation of ferrosomes[15] —
106 organelles involved in storage and detoxification of iron[21,22]. The abundance and appearance of
107 ferrosomes in electron microscopy obscure magnetosomes, making it impossible to visualize
108 the early stages of magnetite biomineralization. To overcome this limitation, we sought an
109 alternative method of magnetosome inhibition that avoids iron starvation.
110 Serendipitously, we discovered that growth in hydrogen instead of nitrogen headspace
111 significantly reduces RS-1's magnetic response (measured as the coefficient of magnetism
112 (C_{mag})[23]) (Figure 2A). A trace C_{mag} at high hydrogen concentrations suggested the need for
113 hydrogen exposure throughout the culture medium. To test this, we flushed both the headspace
114 and medium with 5% hydrogen and grew cells while spinning. Under these conditions, cultures
115 showed no magnetic response as indicated by a C_{mag} of 1 (Figure 2B), and absence of
116 magnetosomes when viewed by transmission electron microscopy (TEM) (Figure 2C).
117 One explanation for these observations is that hydrogen inhibits RS-1 growth, indirectly
118 preventing magnetosome formation. However, growth measurements showed similar final cell
119 densities in hydrogen and nitrogen (Figure 2D), with hydrogen-grown cells exhibiting faster
120 doubling times (6 vs. 8 hours) (Figure 2D). Another possibility is that hydrogen limits iron
121 uptake, restricting magnetosome production. To test this, we used the post-iron-starvation
122 accumulation of ferrosomes as a proxy for iron uptake. Cells were grown in hydrogen and iron-
123 limiting conditions and subsequently exposed to iron with either a nitrogen or hydrogen
124 headspace. Ferrosomes were formed in both nitrogen and hydrogen (Figure 2E *iii* and *iv*), but
125 magnetosomes formed only in nitrogen conditions (Figure 2E-*iv*). This indicates hydrogen does
126 not inhibit iron uptake. Finally, we showed that hydrogen growth does not have a significant
127 impact on the global expression of magnetosome proteins as compared to nitrogen growth
128 conditions. Thus, the mechanisms for inhibition of biomineralization under hydrogen growth
129 conditions remain unresolved (See extended results).
130
131 **Characteristics of early and late stages of biomineralization**
132 We next hypothesized that switching from hydrogen to nitrogen conditions under iron
133 replete conditions could restore magnetosome formation without ferrosome interference. To test
134 this, RS-1 was grown with 10% hydrogen to eliminate magnetosomes, then transferred to
135 nitrogen infused medium. As predicted, magnetic response increased over time (Figure 2F), no

136 ferrosomes were formed, and only magnetosomes were observed (Figure 2G *i-iii*). This
137 transition provides a reliable method to synchronize magnetosome formation and study
138 biomineralization.
139 To capture early stages of biomineralization, RS-1 was incubated shaking in hydrogen-
140 infused medium for several passages to eliminate existing magnetosomes (Figure 2B-*i*). Cells
141 were then transferred to nitrogen-infused medium and harvested once a measurable magnetic
142 response (C_{mag} 1.05-1.15) was detected. Early timepoints in biomineralization showed an
143 average of 3 magnetosomes per cell (Figure 3A, 3C). Many cells contained both mature and
144 immature crystals (Figure 3A-*ii* and *iv*). The median crystal length was 38 nm, with a bimodal
145 distribution indicating both immature and mature crystals present (Figure 3D). Similarly, the
146 shape factor (width-to-length ratio) followed a bimodal pattern, with peaks around 1 for
147 immature and 2 for mature crystals (Figure 3E). During the late stages of biomineralization (C_{mag}
148 1.3-1.5), cells contained complete magnetosome chains composed of smaller subchains (Figure
149 3B), averaging 12 crystals per cell (Figure 3C), all localized to the positive cell curvature. The
150 average crystal length was 51 nm with a shape factor of 1.7, both fitting a normal distribution
151 due to presence of fewer immature crystals (Figure 3D, 3E). These findings point to a crystal
152 growth pattern similar to that proposed for other deep-branching MTB[24]. RS-1 crystals nucleate
153 and grow equidimensionally to approximately 30 nm before elongating anisotropically at one
154 end to produce a tooth-shaped morphology (Figure 3G). High-magnification TEM images
155 revealed two mature magnetosome morphologies: curved and straight which may indicate
156 divergent paths of crystal growth during the elongation step (Figure 3F v to 3F x). However,
157 additional analysis is required to confirm whether these are true characteristics of the 3D
158 crystals, since the images in this study capture only 2D projections.
159 While observing biomineralization stages, we discovered that subcellular magnetosome
160 location correlates with crystal maturation. In early stages, nearly all mature crystals are
161 positioned at the positive cell curvature, where magnetosome chains typically form, but only
162 about 25% of immature crystals are located there (Figure 3H, 3I).
163
164 **Distinct proteomes differentiate early- and late-stage magnetosomes**
165 We next investigated if specific cohorts of proteins are associated with distinct
166 biomineralization stages. Cells from early and late stages were harvested and lysed, and
167 magnetosomes were isolated using a magnetic column. Proteomic analysis of cell lysates and
168 magnetosome fractions via liquid chromatography-mass spectrometry focused on RS-1 MGC-
169 encoded proteins enriched at each stage. Early-stage magnetosomes were enriched for Mad10,

170 MamB, MamA, Mad4, FmpA, FmpB, and MamEO-Cter (Figure 3J), many of which contain
171 predicted transmembrane domains (Supplemental Figure S1 A). Late-stage magnetosomes
172 were enriched for Mad20, Mad23, Mad28, and MamK, all of which lack transmembrane
173 domains (Supplemental Figure S1 A). The actin-like proteins, Mad28 and MamK (Supplemental
174 Figure S1 A), may have roles in chain alignment and organization based on previous work in
175 Alphaproteobacterial MTB[25]. These results suggest a shift in membrane association and chain
176 organization from early to late stages.
177
178 **Early magnetosome proteins regulate biomineralization activity**
179 We next turned to genetics to provide functional evidence for stage-specific action of
180 magnetosome proteins. Previous studies using chemical and UV mutagenesis identified RS-1
181 mutants with severe biomineralization defects, including several alleles of *mamB* that lack a
182 magnetic response and do not produce crystals[12]. This phenotype corroborates our finding that
183 MamB preferentially associates with early-stage magnetosomes (Figure 3J).
184 In contrast to *mamB*, mutants in *fmpA* and *fmpB* can still produce some magnetic
185 particles[12]. FmpA has a transmembrane domain, whereas FmpB contains a signal peptide. Both
186 proteins share serine protease and denitrogenase Fe-Mo domains and are enriched on
187 magnetosomes in the early stages of biomineralization (Supplemental Figure S1 A and Figure
188 3J). Interestingly, the mutations in both *fmpA* and *fmpB* are predicted to eliminate their
189 respective denitrogenase Fe-Mo domains (Figure 4 and Supplemental Figure S1 A). Detailed
190 TEM analysis revealed distinct defects for each strain: *fmpA* mutants produce misshaped
191 circular or symmetrical crystals (Figure 4A, G and Supplemental Figure S2-A), while *fmpB*
192 mutants form smaller wildtype-like (WT-like) crystals, some of which are misshaped (Figure 4B,
193 H and Supplemental Figure S2-B). Consistent with previous findings[12], both mutants exhibit
194 significantly fewer crystals per cell, smaller crystal sizes, and a reduced shape factors as
195 compared to WT (Figure 4D, 4E, and 4F).
196 In addition to the defects in crystal shape and size, *fmpA* and *fmpB* mutants exhibited
197 abnormal crystal placement with most crystals not localized to the cell's positive curvature
198 (Figure 4J). The crystals of the *fmpA* mutant also fail to form chains, while only 5% of *fmpB*
199 mutant cells show chain organization (Figure 4I). These findings suggest FmpA and FmpB are
200 crucial for early magnetosome synthesis and indicate that biomineralization likely initiates away
201 from the positive curvature. We propose that crystal nucleation occurs throughout the cell and
202 crystals are later transported to the positive curvature during the maturation process. Without

203 FmpA and FmpB, crystals could remain "stuck" at nucleation sites, blocking their relocation and
204 preventing new crystal formation, resulting in fewer crystals in mutant cells (Figure 4D).
205
206 **Initiation of chain formation by Mad10**
207 Previous studies identified Mad10 as a magnetite-binding protein[26,27] and hypothesized a
208 role in magnetite nucleation or shape control. We find that Mad10 has the highest abundance
209 ratio among MGC proteins at the magnetosome compared to the cell lysate under all conditions
210 (Supplemental Figure S3 A-C). To investigate its function, we deleted *mad10* in RS-1 via allelic
211 exchange. The Δ*mad10* mutant shows a significantly reduced magnetic response, which is
212 restored by plasmid-based *mad10* expression (Supplemental Figure S4 B and C). Despite the
213 low C_{mag}, however, crystal size and shape remain unchanged and, instead, magnetosomes
214 cluster in a single location within the cell (Figure 5A, Supplemental Figure S4 I and
215 Supplemental Figure S5 A). Crystal numbers also vary widely per cell (Supplemental Figure S4
216 D), likely due to unequal distribution during cell division. These findings indicate that Mad10 is
217 essential for magnetosome chain organization but not for crystal size or shape regulation
218 (Figure 5A).
219
220 **A module of Mad proteins assembles the magnetosome subchain**
221 We next targeted genes encoding proteins more abundant in late stages of
222 biomineralization (Figure 3J) and neighboring genes potentially belonging to the same operon
223 (Figure 1A). All deletions were successfully complemented via plasmid-based expression
224 (Supplemental Figures S4 C, Supplemental Figure S6 A-G). Mutants exhibited a range of chain
225 formation defects which were quantified based on chain placement, magnetosome distribution,
226 and chain/subchain phenotypes (Supplemental Figure S7 F-I).
227 This analysis identified Mad20, Mad23, Mad25, and Mad26 as a module for
228 magnetosome subchain assembly in RS-1. The Δ*mad23* mutant produces the same number of
229 magnetosomes per cell as the WT but they appear dispersed throughout the cell (Figure 5C and
230 Supplemental Figure S4 D). This mutant also has the fewest crystals per subchain among the
231 chain organization mutants and WT resulting in the lowest C_{mag} amongst these strains (Figure
232 5C, Supplemental Figure S4 B, Supplemental Figure S4 E, and Supplemental Figure S5 C).
233 These results suggest that Mad23 connects individual magnetosomes to form subchains. In
234 contrast, the Δ*mad20* mutant forms distinct subchains, some linear, and others in the form of
235 rings, clusters, or curved lines (Figure 5B and Supplemental Figure S5 B). It has fewer
236 subchains than WT (Supplemental Figure S4 F and Supplemental S5 B), but each contains

237 more magnetosomes (Supplemental Figure S4 E). This suggests Mad20 regulates crystal influx
238 into subchains; without it, excess crystals cause curling and distortion (Figure 5B and
239 Supplemental Figure S5 B). Δ*mad25* and Δ*mad26* mutants show similar phenotypes (Figure 5D-
240 E and Supplemental Figure S5 D-E), with crystal and subchain numbers comparable to WT
241 (Supplemental Figure S4 D and F). However, most subchains cluster or form rings, especially in
242 Δ*mad26*, where ~80% cluster and 15% form rings (Supplemental Figure S7 E). These findings
243 indicate Mad25 and Mad26 are essential for maintaining subchain linearity.
244 Overall, these mutants reveal a variety of defects in magnetosome chain assembly and
245 localization in RS-1. Strikingly, many of the mutants exhibit clusters, rings, or curved subchains
246 within the same cell hinting at a lack of long-range connections between these structures. As
247 such, these data suggest that subchains are a fundamental structural unit of chain architecture
248 in RS-1.
249
250 **MamK and Mad28 control subchain separation and chain localization**
251 Mad28 and MamK were selected for genetic analysis due to their higher abundance in
252 late-stage magnetosomes (Figure 3J) and their actin-like domains (Supplemental Figures S1 A
253 and S8). *mamK* is present in nearly all MTB and is well-studied in AMB-1 and MSR-1[28–30]. In
254 AMB-1, *mamK* deletion disrupts chain cohesion[29], creating gaps that affect equal distribution
255 during cell division[31]. In MSR-1, *mamK* deletion results in mislocalized chains, mostly away from
256 the mid-cell[32]. Similarly, in RS-1, we find that MamK plays a role in chain organization. Deletion
257 of *mamK* eliminated the subchain phenotype (Figure 5G, Supplemental Figure S4 F, and
258 Supplemental Figure S5 F), leading to a single continuous chain, which sometimes wrapped
259 around itself, resembling multiple chains. These mutants also had more crystals per cell
260 compared to WT (Figure 5N, Supplemental Figure S4 D).
261 RS-1, and all deep-branching MTB, contain another magnetosome gene, *mad28*, that
262 encodes a protein with an actin-like domain previously suggested to have an overlapping
263 function with MamK[9,25](Supplemental Figure S1 A). Surprisingly, deleting *mad28* in RS-1
264 resulted in a phenotype distinct from that of the Δ*mamK*. In Δ*mad28*, WT-like subchain
265 organization was retained. However, chains were no longer exclusively localized to the positive
266 cell curvature and were found pole-to-pole across the long axis at mid-cell, as well as organized
267 diagonally or transversely across the cell (Figure 5F, 5J, 5K and Supplemental Figure S5 G).
268 To further distinguish between the Δ*mad28* and Δ*mamK* strains, we examined chain
269 formation in a biomineralization time-course experiment. In Δ*mad28*, chain assembly followed
270 the WT pattern, with a single mature crystal forming first, followed by subchain development and

271 crystal incorporation (Figure 5 I-K). However, chains were mispositioned from the start, forming
272 pole-to-pole or diagonal/transverse orientations instead of localizing to the positive cell
273 curvature as in WT (Figure 5 J-K). In contrast, Δ*mamK* exhibited a distinct chain formation
274 pattern. Early biomineralization resembled WT, but as crystals matured, subchains failed to
275 develop, resulting in a single continuous chain (Figure 5L). Δ*mamK* mutants also had more
276 magnetosomes per cell and a higher C_{mag} than WT at both biomineralization stages (Figure 5N,
277 5M, Supplemental Figure S4 B and D), a phenotype not observed in *mamK* mutants of AMB-1
278 and MSR-1[29,32]. These findings suggest that Mad28 aligns magnetosomes to the positive
279 curvature early in chain formation, while MamK distributes subchains along the cell length,
280 ensuring proper alignment and potentially regulating magnetosome production.
281
282 **Interaction Network of chain organization proteins**
283 Bioinformatic analysis shows that Mad10, 20, 23, 25, and 26 contain coiled-coil domains
284 which can facilitate a variety of protein-protein interactions[19] (Supplemental Figure S1 A, S8 C-
285 E). Mad23 also has HEAT repeat domains, known for similar functions (Supplemental Figure S1
286 A and S8 B). Additionally, MamK and Mad28 can form homo- and heteropolymers[25]. Thus, we
287 hypothesized that these chain formation proteins may interact with one another. To explore
288 potential interactions, we conducted Bacterial Adenylate Cyclase Two-Hybrid (BACTH) assays[33]
289 (Figure 6). We created N- and C-terminal fusions to T25 and T18 domains for each protein and
290 tested all interaction combinations (Figure 6 and Supplemental Figure S9). Interactions were
291 classified based on color intensity: dark blue spots as strong (+++), medium blue as moderate
292 (++), and light blue as minor (+) (Figure 6). Our results reveal an extensive and complex
293 network of potential interactions. All proteins exhibited self-interactions in at least one fusion
294 combination. Mad25 was the only protein that interacted with all other proteins tested, while
295 showing no interaction with the T18 and T25 negative controls (Figure 6, Supplemental Figure
296 S9). Mad20, Mad23, Mad26, and MamK each interacted with three or more proteins. Mad10
297 interacted with itself, Mad23, and Mad25 (Figure 6). Mad28 showed an interaction only with
298 Mad25. Among these, Mad25 and Mad26, both containing extensive coiled-coil domains,
299 displayed a particularly strong interaction. Likewise, Mad25 and Mad23 exhibited a strong
300 interaction, likely driven by the coiled-coil domain of Mad25 and the HEAT domain of Mad23
301 (Supplemental Figure S1A, S8B, and S8D). Despite the artificial nature of the BACTH assay,
302 these findings provide further evidence for the existence of a distinct chain organization pathway
303 in deep-branching MTB, dependent on the interactions of coiled-coil and actin-like proteins.
304

305 **A model for magnetosome formation in RS-1**

306 The phenotypic and molecular data presented here suggest a new model for the temporal
307 development of magnetosome chains in RS-1 with the following steps (Figure 7):
308 **Step 1: Nucleation and growth.** Biomineralization initiates at randomly distributed sites within
309 the cell. Mutations in *fmpA* and *fmpB* impair crystal maturation, reduce crystal numbers, and
310 disrupt localization to the positive curvature, linking biomineralization to chain formation. **Step 2:**
311 **Crystal maturation and localization.** As crystals mature, they are transported to the cell's
312 positive curvature. Mad10, previously shown to interact with magnetite[26], may facilitate this
313 transition. Bacterial two-hybrid results suggest an assembly pathway where Mad10 interacts
314 with Mad23 and Mad25 which mediate subsequent steps. **Step 3: Subchain assembly.**
315 Initially, one or two mature crystals appear at the positive curvature. Mad23, in conjunction of
316 Mad25 and Mad26, links accumulating crystals to form and stabilize subchains. **Step 4: Chain**
317 **elongation and positioning.** In parallel to the previous steps, biomineralization sites are
318 distributed along the cell length by MamK, while Mad28 ensures the localization of subchains to
319 the positive curvature. Interestingly, RS-1 MamK and the deep-branching Mad28 can partially
320 complement *mamK* loss in MSR-1[25]. However, our findings suggest that Mad28 mainly controls
321 chain localization, while MamK orchestrates subchain positioning and the number of
322 biomineralization events.
323

324 **Discussion**

325 Magnetotactic bacteria and their magnetosome organelles present an ideal test case to
326 uncover the mechanisms that underly the diversification of specific microbial traits. In recent
327 years, an explosion of genomic and metagenomic studies have revealed that a core
328 magnetosome gene set is often associated with accessory genes that are unique to specific
329 phylogenetic families of MTB. Bioinformatic and structural prediction programs, as well as
330 heterologous expression of these genes in established model systems, have not been
331 successful in determining their role in magnetosome formation. Here, we deployed a new
332 workflow to monitor the process of biomineralization in *D. magneticus* RS-1, a representative of
333 deep-branching MTB, to reveal a distinct mode of organelle assembly mediated by a suite of
334 accessory Mad proteins.

335 Several features of the RS-1 biomineralization and magnetosome chain formation
336 process distinguish it from the model Alphaproteobacterial MTB. First, in RS-1 crystals are
337 made serially, one or a few at a time. AMB-1 and MSR-1, however, produce multiple crystals in
338 parallel[34,35]. Second, biomineralization is a pre-requisite for localization of crystals to the positive

339 cell curvature in RS-1. In contrast, in AMB-1 magnetosome membranes are localized to the
340 positive cell curvature even prior to the initiation of biomineralization[34]. And, while magnetic
341 interactions play a role in chain assembly in MSR-1, mutants with severe biomineralization
342 defects are still able to localize magnetosomes to the positive cell curvature. Third, we notice a
343 shift in the RS-1 magnetosome proteome across the stages of biomineralization. Since
344 proteomic studies in AMB-1 and MSR-1 have been conducted at fixed timepoints, the
345 quantitative shifts in their proteomes across biomineralization timepoints remain unknown. The
346 closest parallels to our work with RS-1 come from a study in AMB-1 that separated
347 magnetosomes based on their magnetic properties leading to the identification of MamY as a
348 protein associated with smaller magnetite particles[36]. Additionally, proteomic comparisons of
349 WT AMB-1 and a mutant lacking MamE protease activity show that despite a severe
350 biomineralization defect the magnetosome protein content was essentially the same between
351 the two strains[37]. An alternative to proteomics has been to visualize the localization of
352 fluorescently tagged proteins in AMB-1 and MSR-1. While most proteins examined maintain a
353 constant magnetosome localization, a handful of proteins, such as Mms6, MamD, and McaB,
354 only localize to magnetosomes of AMB-1 after the initiation of biomineralization[38–40]. However,
355 even these proteins seem to be at magnetosomes from the earliest stages of magnetite
356 formation in clear contrast to the shifting proteome of RS-1 magnetosomes during the
357 biomineralization process. Based on these circumstantial observations, we hypothesize that a
358 similar proteomic transition does not occur in the Alphaproteobacterial MTB.
359 Notably, many of the proteins associated with the early biomineralization stages in RS-1
360 contain predicted transmembrane domains indicating the presence of a magnetosome
361 membrane (Supplemental Figure S1 A). Indeed, previous chemical and UV mutagenesis of RS-
362 1 identified transmembrane-domain-containing proteins such as MamB, MamL, MamQ, Mad2,
363 Mad4,and FmpA as critical players in the early stages of biomineralization[12]. Magnetosome
364 proteins enriched in later stages of RS-1 biomineralization do not contain predicted
365 transmembrane domains and are instead enriched for coiled-coil and actin-like domains
366 (Supplemental Figure S1 A). A global examination of the domain architecture of magnetosome
367 proteins provides further evidence for the potentially distinct role of the magnetosome
368 membrane in each MTB group. For instance, 65% of AMB-1 magnetosome proteins, but only
369 39% RS-1's, are predicted to contain transmembrane domains (Supplemental Figure S10 A-B).
370 However, approximately ~26% (10 proteins) of RS-1 magnetosome proteins contain predicted
371 coiled-coil domains, in contrast to ~12% (6 proteins) of AMB-1's magnetosome proteins
372 (Supplemental Figure S10 C and D). In fact, all of AMB-1's coiled-coil-domain-containing

373 magnetosome proteins, and none of RS-1's, are predicted to contain transmembrane domains
374 (Supplemental Figure S10). This is consistent with previous findings that noted an absence of a
375 magnetosome membrane around mature crystals in RS-1[15]. However, it is also possible that
376 these late proteins are interacting with cytoplasmic domains of transmembrane domain proteins
377 embedded in a magnetosome membrane that is hard to detect. In contrast, lipid-bilayer
378 membranes surrounding mature magnetic particles can be readily observed in a variety of
379 Alphaproteobacterial MTB[34,35,41].
380 Our genetic analysis of several *mad* genes, along with *mamK*, revealed a variety of
381 chain formation defects. Based on the observed phenotypes and bacterial two-hybrid data, we
382 hypothesize that these Mad proteins promote a series of homo- and/or hetero-polymeric
383 reactions to assemble individual magnetic particles into subchains and separate subchains
384 across the long axis of the cell. Notably, other than MamK, all known magnetosome chain
385 formation factors of AMB-1 and MSR-1 (MamJ, MamY, LimJ, MamK-like, McaA, McaB, and
386 MamF and its homologs) are absent in RS-1[28,40,42–45]. Similarly, MTB of the deep-branching
387 *Elusimicrobiota* phylum members which do not form organized magnetosome chains are
388 missing MamK as well as the chain formation Mad proteins. While genome incompleteness
389 should be considered, the two *Elusimicrobiota* genomes show completeness levels of 75.84%
390 and 94.38% in GTDB[8,46]. Therefore, we suggest that these coiled-coil proteins along with the
391 actin-like MamK and Mad28, represent a mechanistic mode of chain organization exclusive to
392 deep-branching MTB.
393 Although the specific proteins involved in chain organization in RS-1 differ from those of
394 Alphaproteobacterial MTB, similar deletion phenotypes can be observed across these distantly
395 related species. For example, deletion of *mad10* in RS-1 produces a phenotype mirroring that of
396 *mamJ* deletion in MSR-1 and the triple deletion missing *mamJ, limJ,* and *mcaA* in AMB-1[40]—all
397 resulting in magnetosome clustering. Similar to Mad10, MamJ was originally hypothesized to be
398 involved in biomineralization due to the presence of a highly acidic domain[35]. However, this
399 domain is not involved in chain organization activity of MamJ and its ability to bind magnetite is
400 unknown[47]. Other mutants also carry superficial phenotypic similarity between RS-1 and AMB-
401 1/MSR-1. For instance, deletion of *mamK* in RS-1 and the loss of *mcaA/mcaB* in AMB-1 lead to
402 loss of subchains in both organisms. The scattered magnetosomes of Δ*mad23* mutant of RS-1
403 also resemble the chain formation defects of the Δ*F3* mutant of MSR-1[42]. These findings
404 indicate that non-homologous proteins may fulfill analogous roles in different MTB groups. They
405 also suggest that disruptions in the organization of a chain of magnetic particles can lead to
406 similar final outcomes.

407 Collectively, our findings shed further light on the evolution and diversification of
408 magnetosomes. Nearly all MTB share genes involved in membrane formation (*mamQ*), iron
409 transport (*mamB*), and chain organization (*mamK*), likely forming the foundations of an ancient
410 iron-accumulating organelle. Diverse magnetosome phenotypes, such as crystal shape
411 variations, may have emerged through addition of subgroup-specific proteins to this core
412 system. In our model, Alphaproteobacterial MTB developed a system to align magnetosome
413 membranes into chains using Mam proteins, while RS-1 and other deep-branching MTB
414 evolved to organize biominerals into chains using Mad proteins. This evolutionarily distinct
415 solution may have arisen to combat the previously described conflict between
416 magnetocrystalline orientation of tooth-shaped magnetosomes and their function as a
417 navigational tool[48,49].
418
419 **Methods**
420
421 **Multiple-sequence alignments and tree construction**
422 Dataset was designed by searching IMG/MER[50] for all known MTB species with
423 homologs for all five of the core *mam* genes selected: *mamA*, *mamB*, *mamE, mamI* and *mamQ.*
424 Next, the dataset was refined to encompass only species with available genomes and
425 accessible TEM images, enabling the identification of magnetosome gene sets (*mam*, *mms*,
426 *mad*, *man* and *mae*) for each species, along with their respective crystal shapes and
427 compositions. Supplemental Table 1 is a list of all species included in designing the
428 phylogenetic tree for this analysis. Once the dataset was complete, the 16S DNA sequences for
429 each species were obtained from NCBI or IMG-M [50] (Supplemental Table 1). Sequences were
430 aligned using MAFFT version 7.490 using the scoring matrix 1PAM/ k=2 [51]. Next, the aligned
431 sequences were used to generate the maximum likelihood tree using PhyMLTree version
432 3.3.20180621 using GTR substitution model with 1000 bootstraps [52]. Additionally, the tree was
433 rooted with *Omnitrophus magneticus* SKK-01.
434
435 **General Culturing for RS-1**
436 *Desulfovibrio magneticus* RS-1 strains were grown at 30°C anaerobically in RS-1 growth
437 medium (RGM), as described previously[12,15]. For growth with hydrogen, the medium was
438 gassed with 10% hydrogen balanced with Nitrogen prior to autoclaving the medium.
439 Additionally, after inoculating, the headspace was re-gassed with the same concentration of
440 hydrogen/nitrogen gas mixture for 10 minutes. All hydrogen cultures were grown spinning on a

441 wheel in the 30°C incubator. Cultures with nitrogen in the headspace that were used as controls
442 for these hydrogen cultures were grown on a wheel in the incubator. All other nitrogen cultures
443 were grown without shaking.
444 For experiments with different concentrations of hydrogen (Figure 2A), RS-1 WT strain
445 was grown at 30°C anaerobically in RS-1 growth medium (RGM), as described above. Initially,
446 all culture tubes were purged with nitrogen gas. Subsequently, prior to inoculation, varying
447 volumes of nitrogen from the headspace were displaced and substituted with an equivalent
448 volume of 100% hydrogen gas, aiming to achieve distinct concentrations of hydrogen in the
449 headspace. Afterwards, RS-1 was inoculated into the culture tubes. Optical density and
450 magnetic response via C_{mag} was monitored throughout growth as previously described [12] using
451 a Spectronic 20D+ Spectrophotometer.
452
453 **Culturing for proteomics**
454 Cultures for hydrogen vs. nitrogen consisted of 350 mL cultures with 2/3 volume of
455 headspace, which were prepared by gassing either with nitrogen or 10% hydrogen and grown
456 by shaking at room temperature. At late exponential phase, cultures were harvested by
457 centrifugation at 8,000 rpm using the Beckman Model J2-21M/E centrifuge. Cell pellets were
458 stored at -80°C until lysis and preparation for proteomic analysis. To examine different stages of
459 biomineralization, 300 mL initial cultures were grown with hydrogen in the headspace to remove
460 all magnetosomes. C_{mag} was measured as described previously[12] and TEM images were taken
461 of initial cultures to ensure no magnetosomes were present. Then 10 1L bottles of RGM-X
462 medium were prepared by infusing the medium with nitrogen and gassing the headspace with
463 nitrogen. Each of the 3 biological replicates consisted of 10 1L bottles, which were inoculated
464 with the same starting culture. Three bottles were used for late biomineralization, which were
465 inoculated with 10 mL of starting culture, and seven bottles were used for early
466 biomineralization samples, which were inoculated with 20 mL of the starting culture. The
467 cultures were grown in a 30°C incubator and OD and C_{mag} were taken 2X daily. When cultures
468 reached a C_{mag} of 1.05-1.15 seven of the bottles were harvested for early biomineralization
469 samples by centrifugation at 8,000 RPM. Subsequently, when the final 3 bottles had a C_{mag}
470 between 1.30-1.5 they were harvested for late stages of biomineralization samples also by
471 centrifugation at 8,000 RPM. Cell pellets were stored at -80°C until it was time to prepare
472 samples for proteomics. Each biological replicate originated from a single colony, which was
473 inoculated into 200 mL pre-culture bottles grown with hydrogen. Each 200 mL pre-culture was

474 subsequently used to inoculate a set of ten 1L bottles, resulting in three 10L cultures derived
475 from three separate colonies.
476
477 **Collecting proteins associated with magnetosomes using a magnetic column**
478 After harvesting cultures, cell pellets were resuspended in buffer A (25 mM Tris, pH 7.0,
479 100 mM sucrose, 1 µg/mL Leupeptin, 1 µg/mL Pepstatin A, and 1 mM PMSF. Cells were lysed
480 three times at 25 kpi using the Single Shot feature of the Multi Cycle (MC) Cell Disruptor from
481 Constant Systems[53]. Magnetic LS Columns (130-042-401) from Miltenyi Biotec were used to
482 separate the magnetosomes from the cell lysate. Magnetic columns were primed with a wash
483 with buffer A, followed by the attachment of magnets to the outside of the columns.
484 Subsequently, the cell lysate was passed through the column by gravity flow. Flow through
485 fractions were passed over the column two more times and buffer A was used for three
486 additional washes. Following wash cycles, the magnets were detached from the column, and
487 500 µL of buffer A was pipetted into the column. The plunger provided with the column was then
488 to provide additional force to collect all of the magnetosomes. Some of the cell lysate from each
489 sample was also saved as a control. Next, a Bradford assay was conducted on all samples to
490 determine the protein concentration, and if necessary, samples were concentrated during this
491 stage. Finally, all samples were trypsin-digested as previously described[21] to prepare them for
492 liquid chromatography-mass spectrometry, as detailed below.
493
494 **Liquid chromatography-mass spectrometry**
495 Trypsin-digested protein samples were each analyzed in triplicate using an Acquity M-
496 class ultra-performance liquid chromatography (UPLC) system that was connected in line with a
497 Synapt G2-Si mass spectrometer (Waters, Milford, MA) as described elsewhere[21]. Data
498 acquisition and analysis were performed using MassLynx (version 4.1, Waters) and Progenesis
499 QI for Proteomics software (version 4.2, Waters Nonlinear Dynamics). Data were searched
500 against the *Desulfovibrio magneticus* strain RS-1 translated protein database to identify
501 peptides[54].
502
503 **Plasmid and cloning and deletion**
504 All plasmids used in this study for generating deletions and for their complementations in
505 RS-1, as well as for plasmids used in the BACTH assays, are listed in Supplemental Table 3. In-
506 frame deletion vectors targeting *mad10*, *mad20*, *mad23*, *mad25*, *mad26, mad28* and *mamK*
507 were constructed by amplifying upstream and downstream homology regions of RS-1 genomic

508 DNA, using the primers listed in Supplementary Table 3. The homology regions were then
509 inserted into the XbaI site of pAK1127 using the Gibson cloning method. The P*npt -strAB*
510 cassette was subsequently inserted between the upstream and downstream homology regions
511 of the deletion vector. Plasmids were transformed into *Escherichia coli* WM3064 and then
512 transferred to *D. magneticus* RS-1 using conjugation methods as described previously [13]. Allelic
513 replacement of *mad10, mad20, mad23, mad25, mad26, mad28* or *mamK* with *strAB* was
514 achieved with streptomycin selection and using two counterselections, 5-Flurouracil and
515 sucrose. All deletions were confirmed by PCR followed by full genomic Illumina sequencing
516 using SeqCenter (https://www.seqcenter.com).
517 To generate plasmids used to complement deletion strains, the genes *mad10*, *mad20*,
518 *mad23*, *mad25*, *mad26, mad28* and *mamK* were individually amplified using primers listed in
519 Supplemental Table 4 and were cloned into pAK906 (containing the *npt* promoter) and pAK907
520 (containing a *mamA* promoter) using Gibson assembly. Both complementation plasmids for
521 each gene were tested by transformation into the respective RS-1 deletion strain. Each strain,
522 containing different versions of the complementation plasmid, was grown in liquid culture and
523 evaluated by C_{mag} measurements and TEM to determine which provided the best
524 complementation. The plasmid that most effectively restored the phenotype was selected for
525 further experiments.
526 To generate plasmids used in the BACTH studies, *mad10, mad20, mad23, mad25,*
527 *mad26, mad28* and *mamK* were either synthesized by Twist Bioscience
528 (https://www.twistbioscience.com) or PCR amplified using the primers listed in Supplementary
529 Table 4 and were cloned into pKT25 or pKNT25 (the N or the C-termini of the T25 fragment)
530 and pUT18 or pUT18C (the N or the C-termini of the T18 fragment) vectors in frame with the
531 T25 and T18 fragment open reading frames by Gibson assembly.
532
533 **Biomineralization time course using hydrogen**
534 RS-1 strains were grown at 30°C anaerobically, as described above. Initial cultures were
535 all grown with medium infused with 10% hydrogen and headspace was purged again with 10%
536 hydrogen after inoculation. All hydrogen cultures were grown on a wheel in the incubator.
537 Additionally, all cultures were transferred for supplementary growth into hydrogen tubes to
538 ensure the removal of all magnetosomes. Varying volumes (1mL, 0.5 mL, 0.2 mL, and 0.1 mL)
539 of hydrogen grown cultures were transferred into nitrogen-infused medium, aiming to capture all
540 stages of biomineralization more effectively. Optical density and magnetic response via C_{mag}
541 was monitored throughout growth as previously described [12] and at different stages of

542 biomineralization samples were saved for TEM imaging. The progression of biomineralization
543 stages was tracked using C_{mag}, with values ranging from 1.05 to 1.10 classified as early stages,
544 1.15 to 1.20 as middle stages, and 1.3 to 1.6 as late stages.
545
546 **Bacterial adenylate cyclase two-hybrid (BACTH) assays**
547 The assay was performed as described in the Euromedex BACTH system kit manual. N-
548 and C-terminal T18 and T25 fusions of Mad10, Mad20, Mad23, Mad25, Mad26, Mad28 and
549 MamK proteins were constructed using plasmid pKT25, pKNT25, pUT18C, and pUT18 in *E. coli*
550 K12 strain DH5-alpha. All plasmids were sequence-verified to show T18/T25 magnetosome
551 protein fusions were correct. The fusions were then co-transformed into competent *E. coli*
552 DHM1 cells (lacking endogenous adenylate cyclase activity) in all pairwise combinations, plated
553 on LB agar plates containing 100 µg/mL carbenicillin and 50 µg/mL kanamycin, and incubated
554 at 30 °C overnight. Several colonies of T18/T25 co-transformants were isolated and grown in LB
555 liquid medium with 100 µg/mL carbenicillin and 50 µg/mL kanamycin overnight at 30 °C with 220
556 rpm shaking. Overnight cultures were spotted on indicator plates containing minimal
557 M63/maltose medium with agar supplemented with 40 µg/mL X-gal, 50 µg/ml carbenicillin; and
558 25 µg/ml kanamycin. Plates were incubated 4 to 8 days at 30 °C before imaging. Bacteria
559 expressing interacting hybrid proteins will show blue, while bacteria expressing non-interacting
560 proteins will remain white. Different concentrations of IPTG (0, 0.1 mM and 0.5 mM) were tested
561 in the overnight culture as well as on the indicator plates with little to no difference. Therefore,
562 IPTG was not included in the final cultures and plates of this experiment. Plates were imaged
563 using a Canon EOS R50 camera with a Canon RF35mm F1.8 Macro STM Lens.
564
565 **Electron microscopy**
566 Whole-cell TEM imaging was performed as described previously [15]. All TEM was done
567 using the Tecnai 12 at the EM-Lab at the University of California, Berkeley (https://em-
568 lab.berkeley.edu/EML/index.php). Magnetosomes were measured manually using ImageJ. Cells
569 were also counted manually.
570
571 **Acknowledgement**
572 A.K. and V.V.R. are supported through the National Institute of General Medical Sciences
573 (R35GM127114). The QB3/Chemistry Mass Spectrometry Facility at the University of California,
574 Berkeley received support from the National Institutes of Health (grant 1S10OD020062-01).
575 Additionally, V.V.R. was supported through the Genetics Training Grant, which receives funds

576 from the National Institutes of Health (Grant #: 1T32GM132022). Thank you to the staff at the
577 University of California Berkeley Electron Microscope Laboratory for advice and assistance in
578 electron microscopy.
579
580

Figures:

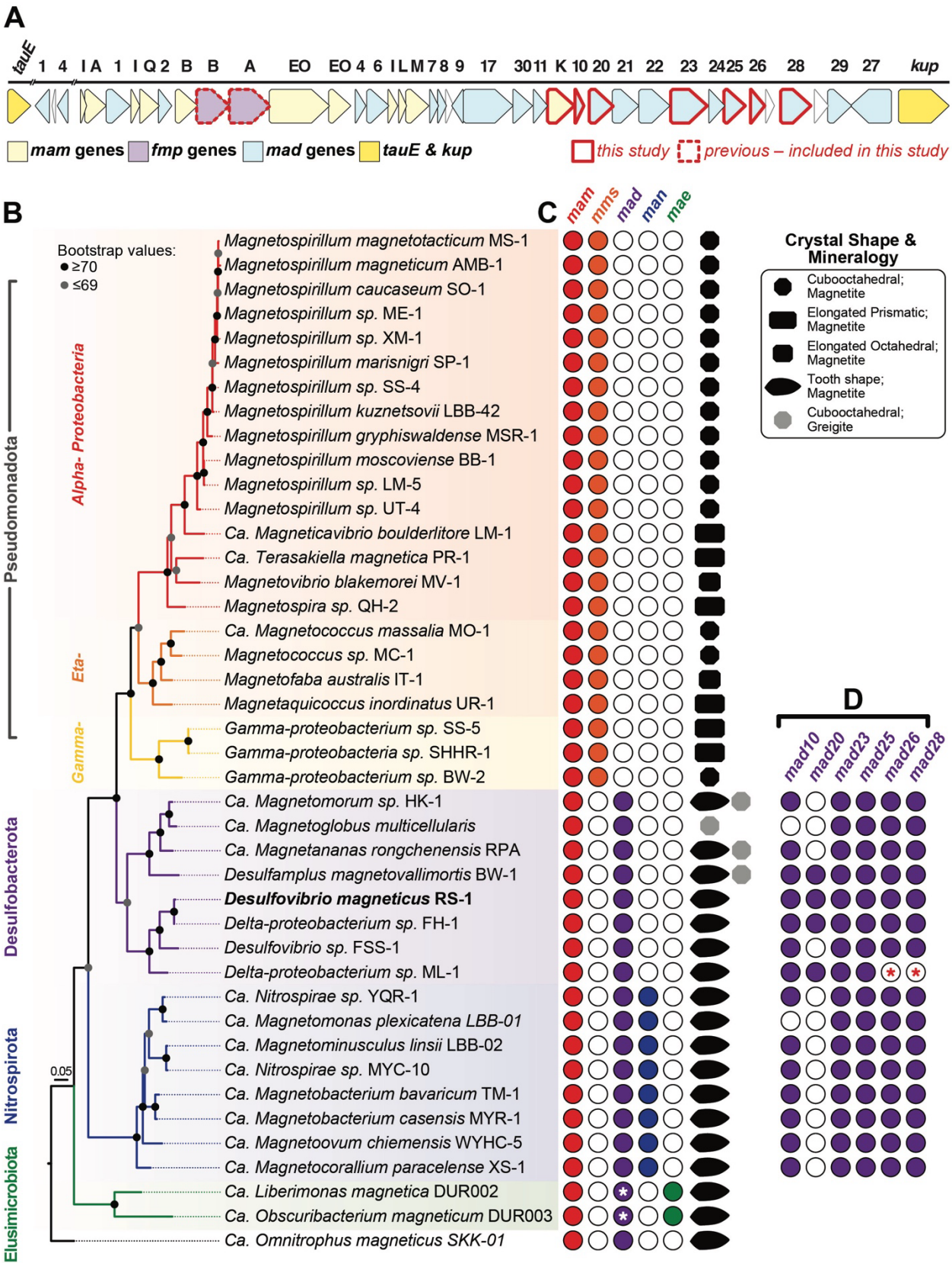
A
tauE
1 4 I A 1 I Q 2 B B A EO EO 4 6 I L M 7 8 9 17 30 11 K 10 20 21 22 23 24 25 26 28 29 27 kup
mam genes
fmp genes
mad genes
tauE & kup
this study
previous – included in this study
B
C
mam
mms
mad
man
mae
Bootstrap values:
≥70
≤69
Pseudomonadota
Alpha- Proteobacteria
Eta-
Gamma-
Desulfobacterota
Nitrospirota
Elusimicrobiota
0.05
Magnetospirillum magnetotacticum MS-1
Magnetospirillum magneticum AMB-1
Magnetospirillum caucaseum SO-1
Magnetospirillum sp. ME-1
Magnetospirillum sp. XM-1
Magnetospirillum marisnigri SP-1
Magnetospirillum sp. SS-4
Magnetospirillum kuznetsovii LBB-42
Magnetospirillum gryphiswaldense MSR-1
Magnetospirillum moscoviense BB-1
Magnetospirillum sp. LM-5
Magnetospirillum sp. UT-4
Ca. Magneticavibrio boulderlitore LM-1
Ca. Terasakiella magnetica PR-1
Magnetovibrio blakemorei MV-1
Magnetospira sp. QH-2
Ca. Magnetococcus massalia MO-1
Magnetococcus sp. MC-1
Magnetofaba australis IT-1
Magnetaquicoccus inordinatus UR-1
Gamma-proteobacterium sp. SS-5
Gamma-proteobacteria sp. SHHR-1
Gamma-proteobacterium sp. BW-2
Ca. Magnetomorum sp. HK-1
Ca. Magnetoglobus multicellularis
Ca. Magnetananas rongchenensis RPA
Desulfamplus magnetovallimortis BW-1
Desulfovibrio magneticus RS-1
Delta-proteobacterium sp. FH-1
Desulfovibrio sp. FSS-1
Delta-proteobacterium sp. ML-1
Ca. Nitrospirae sp. YQR-1
Ca. Magnetomonas plexicatena LBB-01
Ca. Magnetominusculus linsii LBB-02
Ca. Nitrospirae sp. MYC-10
Ca. Magnetobacterium bavaricum TM-1
Ca. Magnetobacterium casensis MYR-1
Ca. Magnetoovum chiemensis WYHC-5
Ca. Magnetocorallium paracelense XS-1
Ca. Liberimonas magnetica DUR002
Ca. Obscuribacterium magneticum DUR003
Ca. Omnitrophus magneticus SKK-01
Crystal Shape & Mineralogy
Cubooctahedral; Magnetite
Elongated Prismatic; Magnetite
Elongated Octahedral; Magnetite
Tooth shape; Magnetite
Cubooctahedral; Greigite
D
mad10
mad20
mad23
mad25
mad26
mad28

583 **Figure 1.** *Phylogenetic tree of MTB with their magnetosome gene composition and*
584 *magnetosome crystal shape*
585 (A) Magnetosome gene cluster in RS-1. All *mam* genes are in yellow, all *mad* genes are in blue
586 and *fmp* genes are in purple. Genes outlined in red (*mamK*, *mad10*, *mad20*, *mad23*, *mad25*,
587 *mad26* and *mad28*) were the focus of this study. Outlined in dotted red (*fmpA* and *fmpB*) are
588 genes mutated in a previous study[12], but examined further in this study. (B) 16S maximum
589 likelihood tree. MAFFT was used for alignment of 16S genes. Maximum likelihood tree was built
590 using PhyML Tree[52] with GTR substitution model and 1000 bootstraps. (C) For each MTB
591 species the classification of the type of magnetosome genes (*mam*, *mms*, *mad*, *man* or *mae*)
592 are provided as well as the magnetosome mineral composition and shape. White asterisks
593 indicate the potential presence of *mad* genes, which were previously reported as missing[8] (*see*
594 *Supplemental Figure S1 B*). (D) Deep-branching MTB species that contain the *mad* genes
595 studied here. Red asterisks represent uncertainty due to a lack of a completed genome on
596 NCBI. *Supplemental Table 1* contains all the data (NCBI genome IDs, 16S gene ID and
597 references) used to generate the phylogenetic tree (B), magnetosome gene information (A, C &
598 D), and literature with crystal TEM images and chemical composition (C).

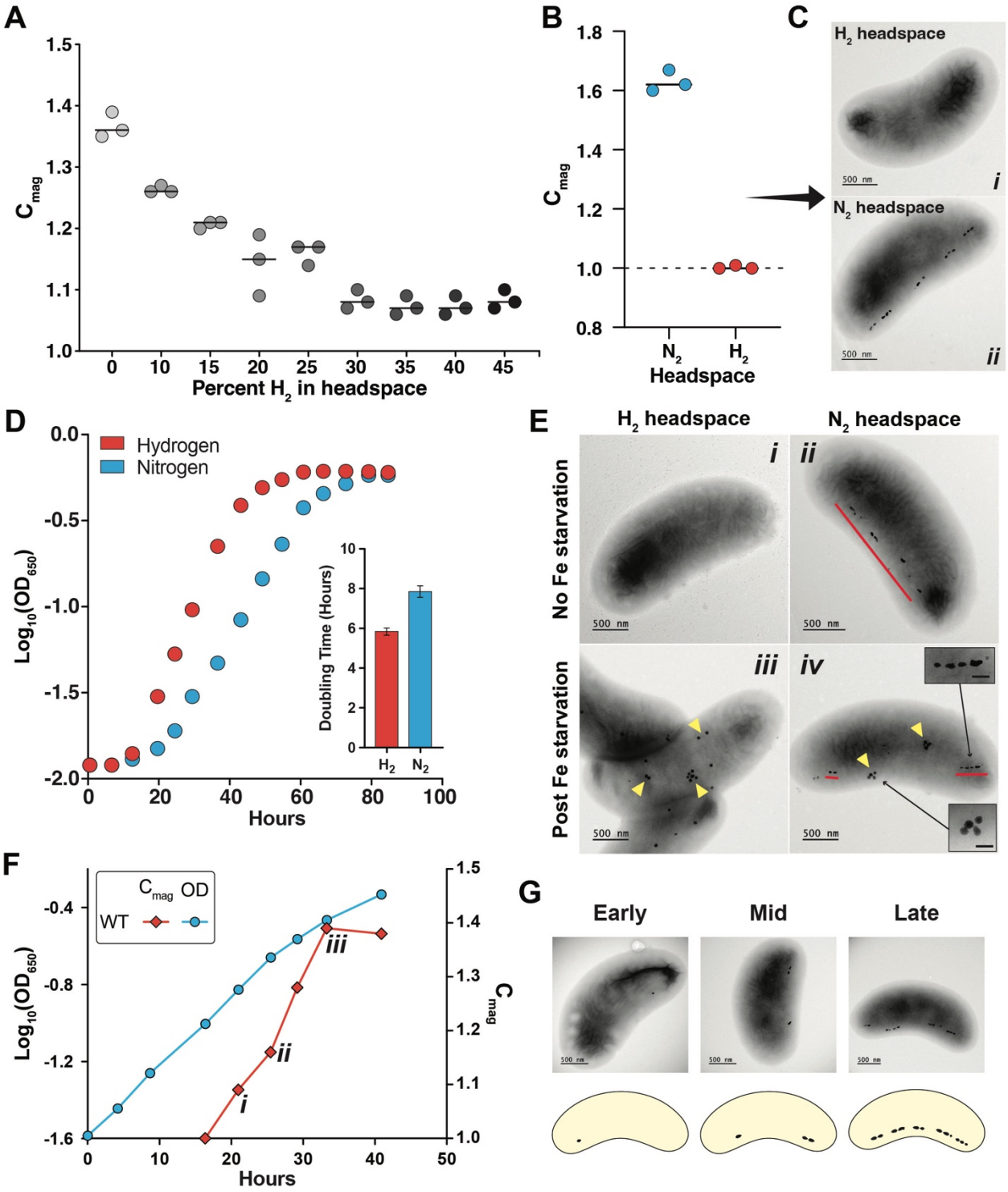

Figure 2. *Hydrogen inhibits magnetosome synthesis but not ferrosome production*

(A) Different concentration of hydrogen gas was added to the headspace and the magnetic response, C_{mag} was measured over growth. (B) Growth curve of WT RS-1 grown with nitrogen (blue) or hydrogen (orange) in the headspace. Inlet graph shows the doubling time for both

604 conditions. (C) RS-1 grown spinning on a wheel with either nitrogen (blue) or hydrogen
605 (orange). C_{mag} values indicate no magnetic response for cultures grown with hydrogen in the
606 headspace. (D) TEM images of cultures from (C). (E) Initial cultures were either grown with or
607 without iron to simulate iron starvation. Pre-cultures were transferred into either hydrogen or
608 nitrogen conditions. (E *i*) TEM image of a cell grown in hydrogen with no iron starvation, (E *ii*)
609 TEM image of a cell grown in nitrogen with no iron starvation, and (E *iii* and *iv*) are TEM images
610 40 hours after iron starvation for cells grown in hydrogen (*iii*) or nitrogen (*iv*). Blue lines indicate
611 magnetosomes and yellow triangles point to ferrosomes. (F) Growth curve (blue line) of a
612 culture transitioning from hydrogen to nitrogen conditions to initiate biomineralization. The C_{mag}
613 curve (orange line) of the same culture demonstrates biomineralization initiation and
614 progression during growth. (F *i-iii*) indicate time points at which samples were collected for TEM
615 imaging in (G *i-iii*).

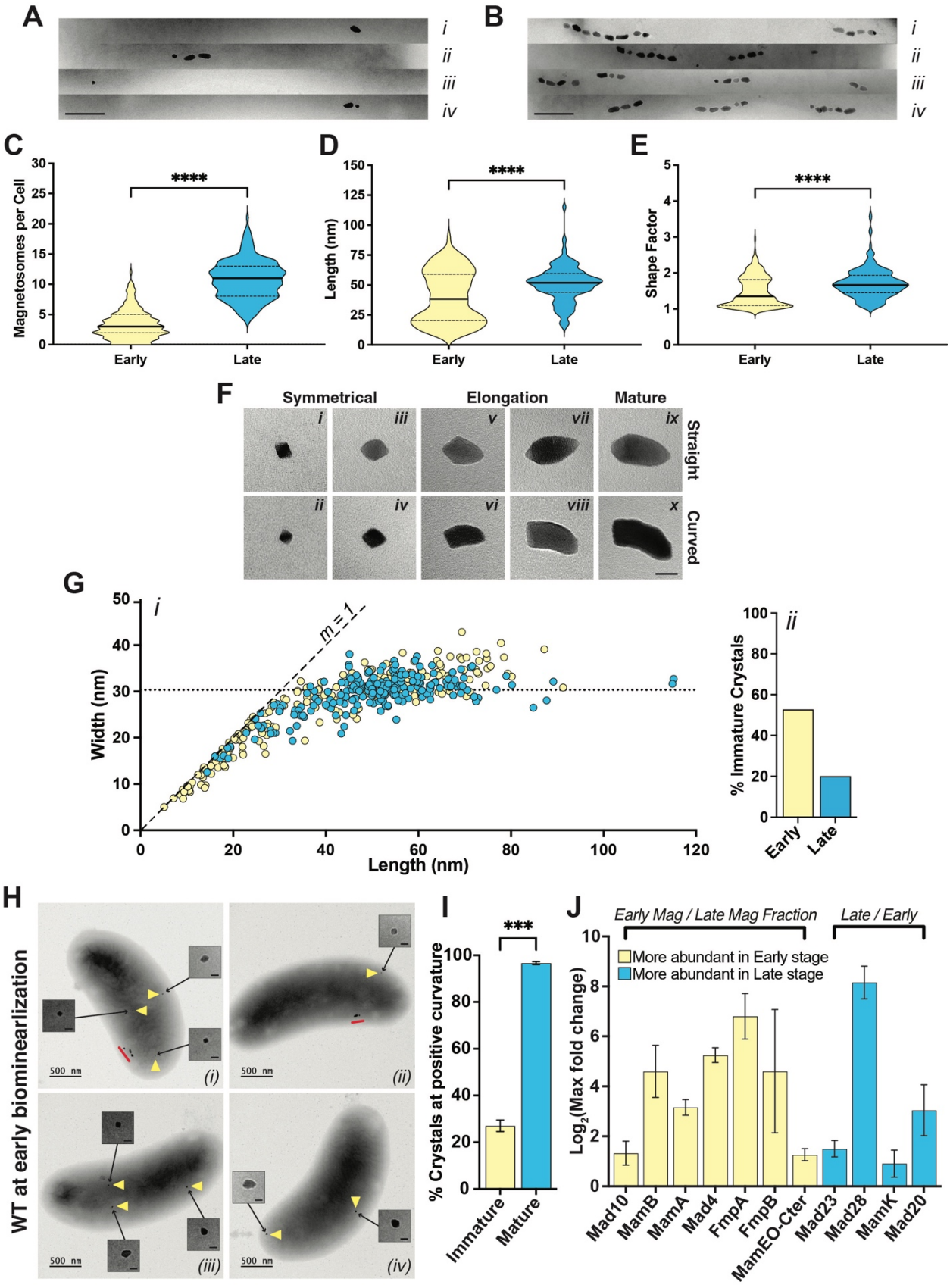
A
i
ii
iii
iv
B
i
ii
iii
iv
C
Magnetosomes per Cell
****
Early
Late
D
Length (nm)
****
Early
Late
E
Shape Factor
****
Early
Late
F
Symmetrical
Elongation
Mature
Straight
Curved
G
i
m = 1
Width (nm)
Length (nm)
ii
% Immature Crystals
Early
Late
H
WT at early biomineralization
500 nm
(i)
(ii)
(iii)
(iv)
I
% Crystals at positive curvature
***
Immature
Mature
J
Early Mag / Late Mag Fraction
Late / Early
More abundant in Early stage
More abundant in Late stage
Log2(Max fold change)
Mad10
MamB
MamA
Mad4
FmpA
FmpB
MamEO-Cter
Mad23
Mad28
MamK
Mad20

616

617 **Figure 3.** *Proteomic analysis of magnetosome proteins at different stages of biomineralization*
618 (A-B) TEM images of chains representing early and late stages of biomineralization, with the
619 scale bars representing 250 nm. (C) Violin plots depicting the number of magnetosomes per cell
620 for cells in early and late stages of biomineralization. (D) Violin plots illustrating measurements
621 of magnetosome length and (E) shape factor (length/width) for crystals found in early and late
622 stages of biomineralization, n=212 for early stages and n=214 for late stages. Statistical tests
623 for panels C–E are listed in Supplemental Table 5. (F) TEM images of RS-1 magnetosomes at
624 different stages of growth. The black scale bar in panel *x*, shown for the zoomed-in crystals,
625 represents 25 nm and applies to panels *i* through *x*. (G) Each point is the measurement of the
626 length and width of one crystal from WT (AK80). Yellow dots represent crystals from cells at
627 early stages of biomineralization. Blue dots represent crystals from cells at late stages of
628 biomineralization. The dotted line represents the median width of crystals from late stages of
629 biomineralization. Dashed line shows a slope (*m*) of 1. (H) TEM images of early stage
630 biomineralization of WT cells. Yellow triangles point to immature crystals that are included as
631 zoomed-in images in the inset. Red lines indicates mature magnetosomes. The scale bars in
632 the insets represents 25 nm and applies to panels *i* through *iv*. (I) The proportion of
633 magnetosomes positioned at the positive curvature of the cell for both immature (yellow bar)
634 and mature (blue bar) crystals during this stage, 140 cells counted; n=254 immature crystals,
635 and n=394 mature crystals and statistical tests for I are listed in Supplemental Table 5. (J) The
636 $\log_2$ maximum fold change of magnetosome protein abundance detected in the magnetosome
637 fraction at different stages of biomineralization. Yellow bars represent proteins more abundant
638 at the early stage and blue bars represent proteins more abundant at the late stage of
639 biomineralization.

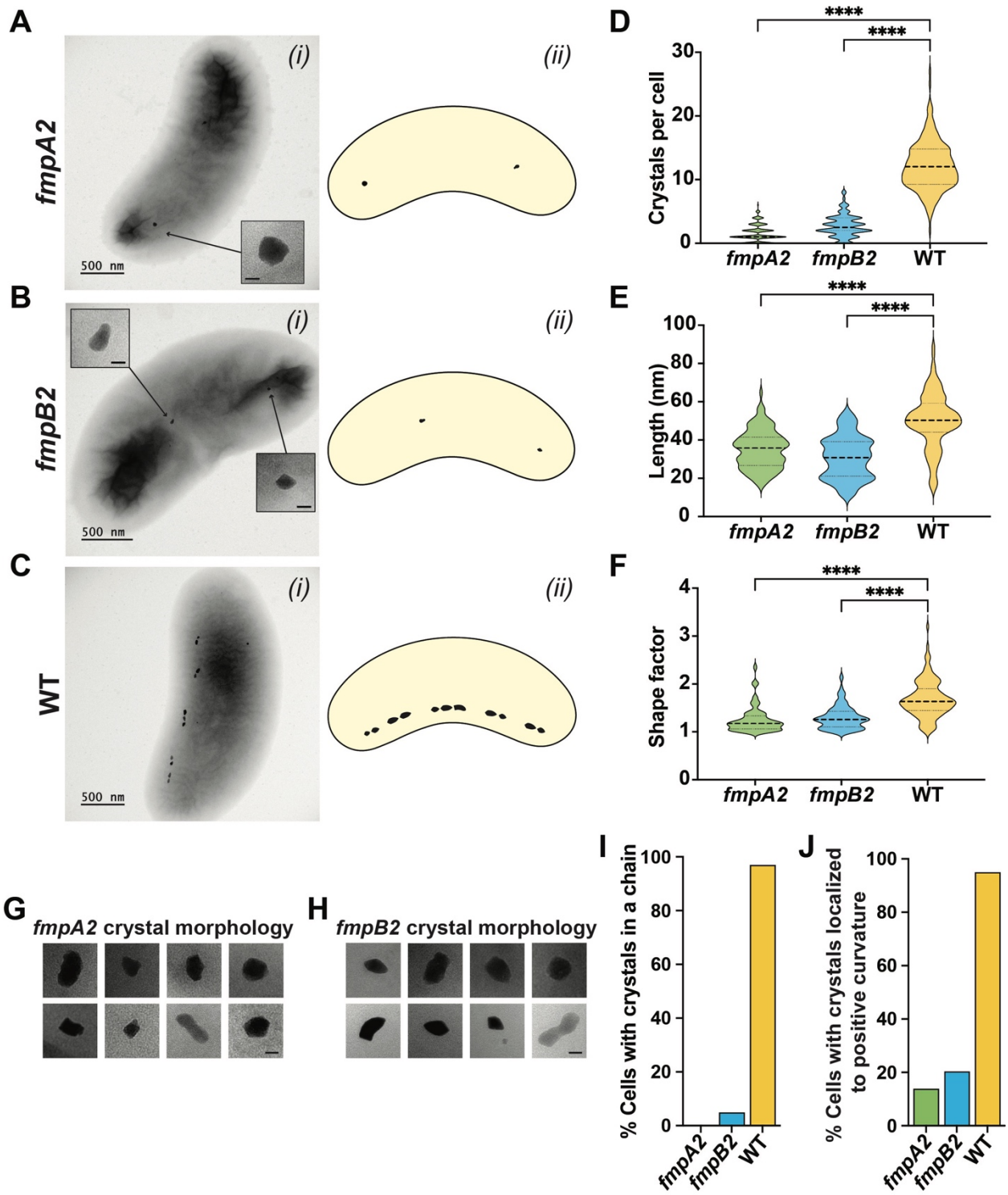

Figure 4. *Characterization of fmpA and fmpB mutants*

A-C) (*i*) TEM images of *fmpA* and *fmpB* mutant strains (scale bars 500 nm for main image and 25 nm for inset). *fmpA2* represents the *fmpA* allele 2 mutant Q418*, where there is a premature stop at amino acid 418 and *fmpB2* represent the *fmpB* allele 2 mutant 808delG, which has a

645 frameshift from a deleted nucleotide at amino acid 270[12] (Supplemental Figure S1 A). (*ii*)
646 Cartoon diagram of each strain. (D) Violin plots depicting the number of crystals per cell for
647 each strain. (E) Violin plots illustrating measurements of magnetosome length, and (F) shape
648 factor (length/width) for crystals in each strain. Panels (D), (E), and (F) are based on n = 200
649 per strain; details of the statistical tests are provided in Supplemental Table 6. (G-H) Crystal
650 morphology for each mutant, scale bars are 25 nm. (I) Percentage of cells exhibiting a chain
651 phenotype, defined as having more than one crystal aligned in a row, for each strain. (J)
652 Percent of cells with crystals located at the positive curvature in the cell. (I-J) Over 200 cells
653 were counted.

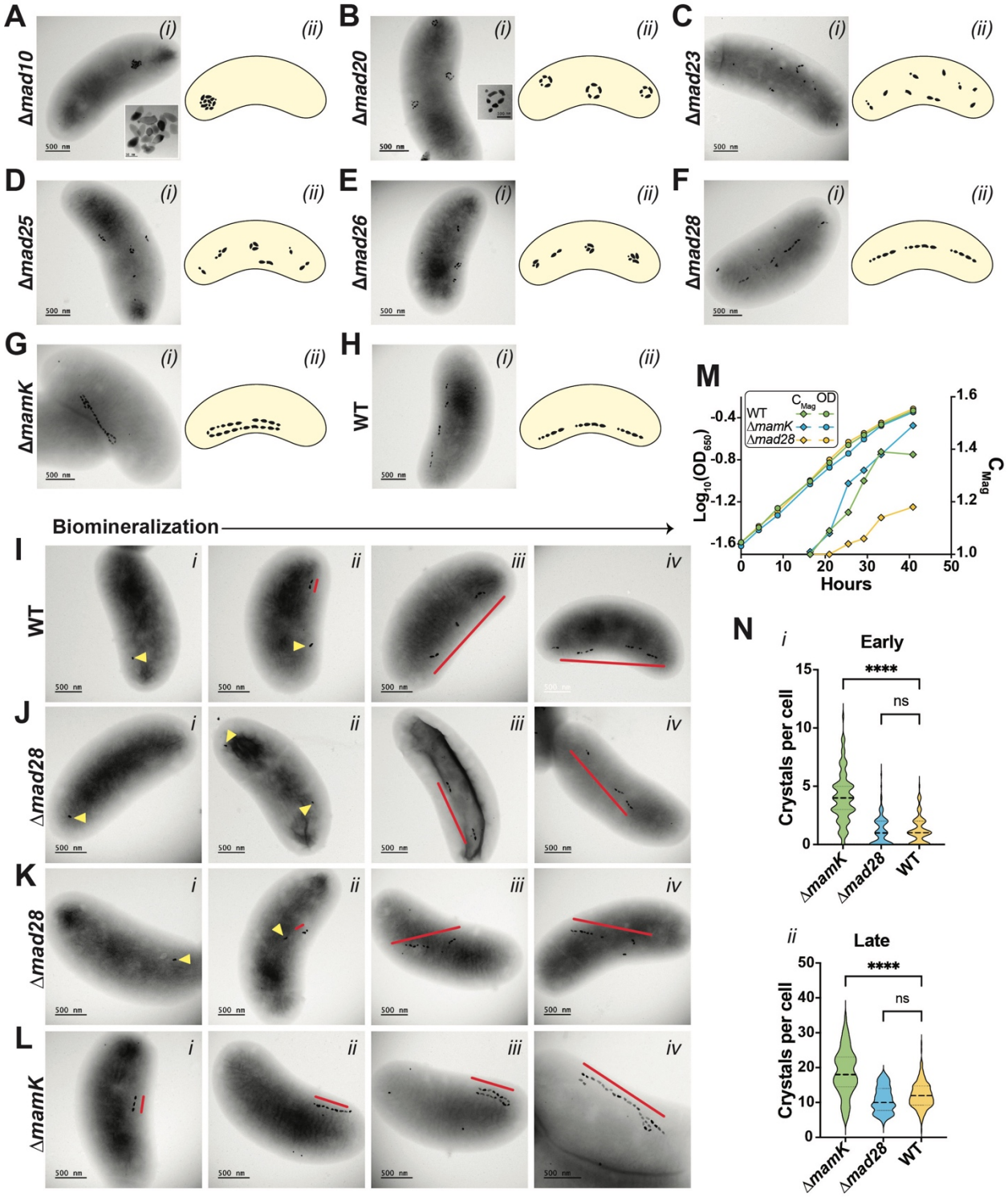

Figure 5. *Deletions of* mad *genes and mamK result in a variety of chain formation and localization defects*

(A-H) Phenotypes of different magnetosome gene deletion mutants and WT RS-1 with scale bars representing 500 nm. (*i*) is a TEM image for each strain and (*ii*) shows a cartoon diagram

659 of representative magnetosome chain morphology. (I-L) TEM images of biomineralization time
660 course of Δ*mad28*, Δ*mamK* and WT with scale bars representing 500 nm. Yellow triangles point
661 at individual magnetosomes, whereas red lines indicate chains or subchains of crystals. (I)
662 Biomineralization time course of WT. (J) shows the phenotype for Δ*mad28* where the chain
663 localizes to the mid-cell, whereas (K) shows the phenotype for Δ*mad28* where the chain
664 localizes diagonally or transversally. (L) Biomineralization time course for Δ*mamK*, shows no
665 subchains forming. (M) Growth curve and C_{mag} curve for WT, Δ*mad28* and Δ*mamK*. (N *i*) Violin
666 plots depicting the number of magnetosomes per cell for WT, Δ*mad28* and Δ*mamK* at early
667 stages of biomineralization, over 100 cells counted for each strain. (N *ii*) Violin plots illustrating
668 the number of magnetosomes per cell for WT, Δ*mad28* and Δ*mamK* at late stages of
669 biomineralization, over 100 cells counted for each strain. Statistical tests for panels N *i-ii* are
670 listed in Supplemental Table 7.
671

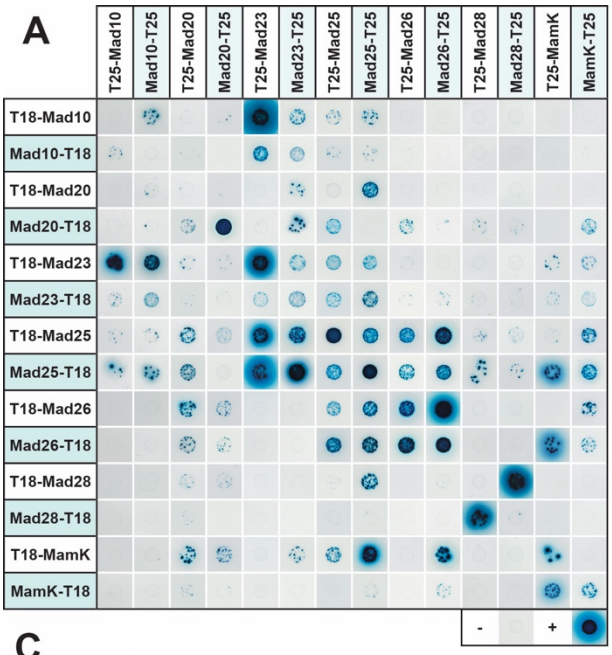

B

	T25-Mad10	Mad10-T25	T25-Mad20	Mad20-T25	T25-Mad23	Mad23-T25	T25-Mad25	Mad25-T25	T25-Mad26	Mad26-T25	T25-Mad28	Mad28-T25	T25-MamK	MamK-T25
T18-Mad10	-	++	-	-	+++	+	+	+	-	-	-	-	-	-
Mad10-T18	+	-	-	-	++	+	+	+	-	-	-	-	-	-
T18-Mad20	-	+	-	-	-	+	-	++	-	-	-	-	-	-
Mad20-T18	-	-	+	+++	-	++	+	-	+	-	+	+	-	+
T18-Mad23	+++	+++	+	+	+++	+	+	+	-	-	-	-	+	+
Mad23-T18	+	+	-	-	+	+	+	++	-	+	-	-	+	+
T18-Mad25	+	+	++	+	+++	++	+++	++	++	+++	+	+	-	++
Mad25-T18	+	++	++	-	+++	+++	++	+++	+	++	++	+	++	++
T18-Mad26	-	-	++	+	-	-	+	++	++	+++	-	-	-	++
Mad26-T18	-	-	++	+	-	-	++	++	+++	+++	-	-	++	+
T18-Mad28	-	-	+	+	-	-	-	++	-	-	-	+++	-	-
Mad28-T18	-	-	-	-	-	-	-	-	-	-	+++	-	-	-
T18-MamK	-	-	++	++	-	+	++	+++	-	++	-	-	++	-
MamK-T18	-	-	+	-	-	-	-	-	-	+	-	-	++	++

C

	Domains	Positive interactions*
Mad10	Coiled-coil	10, **23**, 25
Mad20	Coiled-coil	**20**, 23, 25, 26, K
Mad23	Coiled, Heat	**10**, 20, **23**, **25**
Mad25	Coiled-coil	10, 20, 23, **25**, **26**, 28, **K**
Mad26	Coiled-coil	**25**, **26**, **K**
Mad28	Actin-like	25, **28**
MamK	Actin-like	23, **25**, **26**, **K**

*Strong interactions in Bold

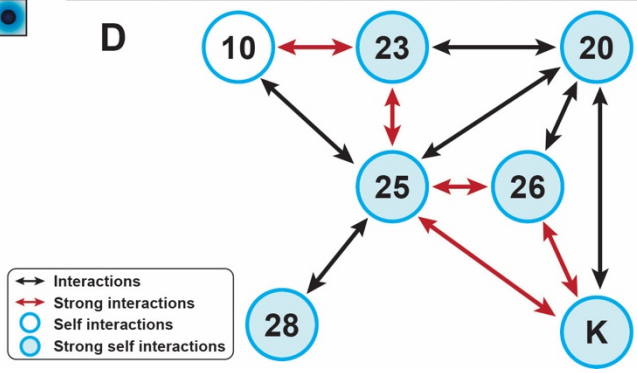

672
673 **Figure 6.** *Interactions of magnetosome chain organization proteins*

A Bacterial Adenylate Cyclase Two-Hybrid (BACTH) assay was conducted to assess interactions among magnetosome chain organization proteins—Mad10, Mad20, Mad23, Mad25, Mad26, Mad28, and MamK. Co-transformed *E. coli* DHM1 expressing T18- and T25-fusion proteins were spotted onto M63 maltose-mineral salts agar, where blue coloration indicates high β-galactosidase activity, signifying a positive interaction, while white indicates no interaction. The positive control (leucine zipper) resulted in dark blue spots, while the negative controls (empty vector combinations) produced white spots, as expected. (A) Photographic images of spots for each interaction combination. (B) A table summarizing all interaction combinations, scored based on results from (A) and categorized by color intensity: dark blue spots indicate strong interaction (+++), medium blue spots represent moderate (++), light blue spots signify minor (+), and white denotes no interaction (-). (C) A table highlighting the interactions. Strong interactions (+++) are indicated in bold. (D) A visual diagram illustrating these interactions: black arrows represent interactions, including bidirectional interactions (fusion with T25 and T18 interacting with their corresponding fusion partners), red arrows highlight stronger bidirectional interactions, open blue circles indicate observed self-interactions, and filled blue circles denote stronger self-interactions.

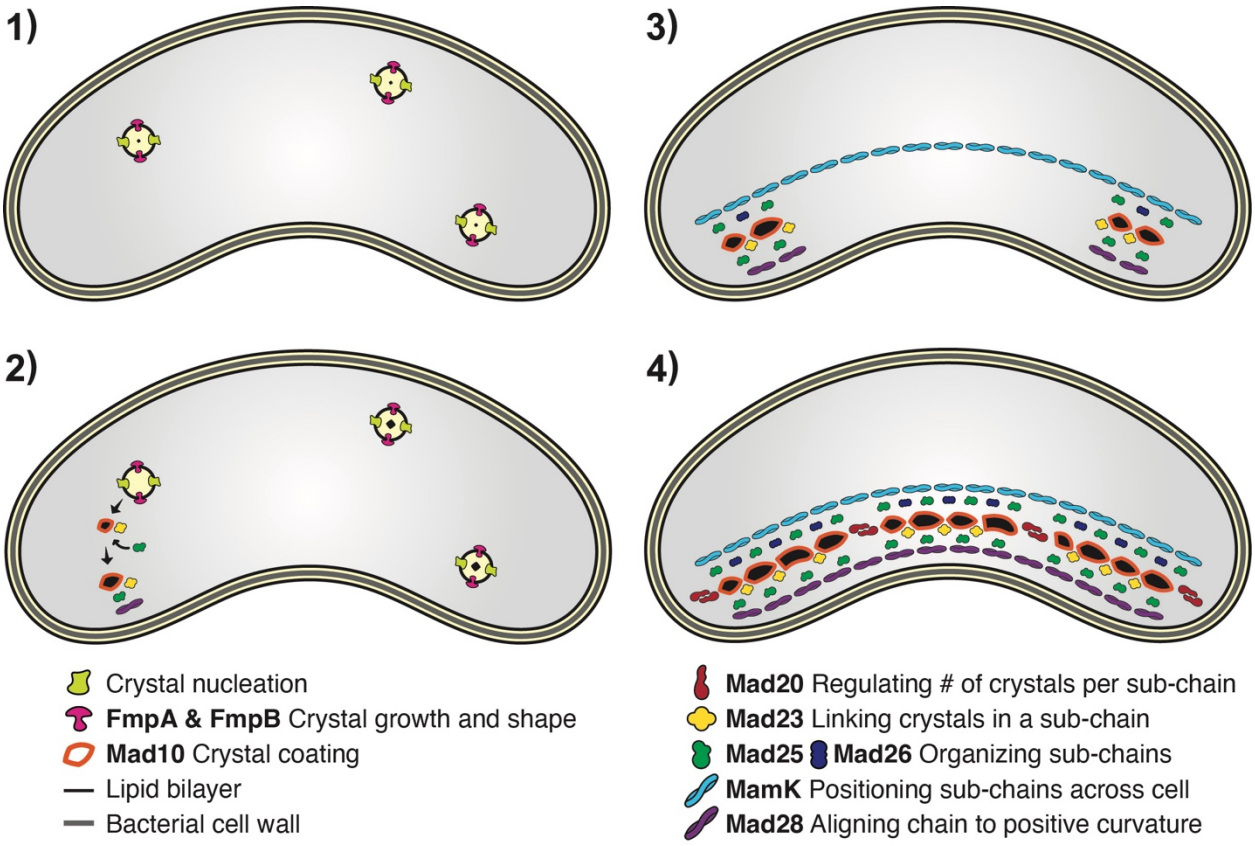

Figure 7. *Model of Magnetosome synthesis and chain organization in RS-1*

692 Model of the different stages of biomineralization in *Desulfovibrio magneticus* RS-1. ***Step 1:***
693 *Nucleation and growth.* Biomineralization begins at nucleation sites randomly distributed within
694 the cell. ***Step 2:*** *Crystal maturation and localization.* Maturing crystals are transported to the
695 cell's positive curvature by a cohort of Mad proteins. ***Step 3:*** *Subchain assembly.* As crystals
696 reach the positive curvature, the process shifts to organizing them into subchains. ***Step 4:***
697 *Chain elongation and positioning.* Subchains are extended and aligned along the cell length by
698 MamK, while Mad28 ensures the chain remains localized at the positive curvature.
699

700

701 **References:**

702

703 1. Amor, M., Mathon, F. P., Monteil, C. L., Busigny, V. & Lefevre, C. T. Iron-biomineralizing
704 organelle in magnetotactic bacteria: function, synthesis and preservation in ancient rock
705 samples. *Environ. Microbiol.* **22**, 3611–3632 (2020).
706 2. Wan, J. *et al.* Biomineralization in magnetotactic bacteria: From diversity to molecular
707 discovery-based applications. *Cell Rep.* **43**, 114995 (2024).
708 3. Lefevre, C. T. & Bazylinski, D. A. Ecology, Diversity, and Evolution of Magnetotactic
709 Bacteria. *Microbiol. Mol. Biol. Rev.* **77**, 497–526 (2013).
710 4. Amor, M. *et al.* Magnetotactic Bacteria Accumulate a Large Pool of Iron Distinct from Their
711 Magnetite Crystals. *Appl. Environ. Microbiol.* **86**, e01278-20 (2020).
712 5. Vargas, G. *et al.* Applications of Magnetotactic Bacteria, Magnetosomes and Magnetosome
713 Crystals in Biotechnology and Nanotechnology: Mini-Review. *Molecules* **23**, 2438 (2018).
714 6. Lin, W. *et al.* Genomic expansion of magnetotactic bacteria reveals an early common origin
715 of magnetotaxis with lineage-specific evolution. *ISME J.* **12**, 1508–1519 (2018).
716 7. Kolinko, I. *et al.* Biosynthesis of magnetic nanostructures in a foreign organism by transfer
717 of bacterial magnetosome gene clusters. *Nat. Nanotechnol.* **9**, 193–197 (2014).
718 8. Uzun, M. *et al.* Recovery and genome reconstruction of novel magnetotactic Elusimicrobiota
719 from bog soil. *ISME J.* **17**, 204–214 (2023).
720 9. Liu, P. *et al.* Key gene networks that control magnetosome biomineralization in
721 magnetotactic bacteria. *Natl. Sci. Rev.* **10**, nwac238 (2023).
722 10. Sakaguchi, T., Burgess, J. G. & Matsunaga, T. Magnetite formation by a sulphate-reducing
723 bacterium. *Nature* **365**, 47–49 (1993).

724 11. Sakaguchi, T., Arakaki, A. & Matsunaga, T. Desulfovibrio magneticus sp. nov., a novel
725 sulfate-reducing bacterium that produces intracellular single-domain-sized magnetite
726 particles. *Int. J. Syst. Evol. Microbiol.* **52**, 215–221 (2002).
727 12. Rahn-Lee, L. *et al.* A Genetic Strategy for Probing the Functional Diversity of Magnetosome
728 Formation. *PLoS Genet.* **11**, e1004811 (2015).
729 13. Grant, C. R., Rahn-lee, L. & Legault, K. N. Genome Editing Method for the Anaerobic
730 Magnetotactic. *Appl. Environ. Microbiol.* **84**, 1–12 (2018).
731 14. Nakazawa, H. *et al.* Whole genome sequence of *Desulfovibrio magneticus* strain RS-1
732 revealed common gene clusters in magnetotactic bacteria. *Genome Res.* **19**, 1801–1808
733 (2009).
734 15. Byrne, M. E. *et al. Desulfovibrio magneticus* RS-1 contains an iron- and phosphorus-rich
735 organelle distinct from its bullet-shaped magnetosomes. *Proc. Natl. Acad. Sci.* **107**, 12263–
736 12268 (2010).
737 16. Waldman, V. M., Stanage, T. H., Mims, A., Norden, I. S. & Oakley, M. G. Structural
738 mapping of the coiled-coil domain of a bacterial condensin and comparative analyses across
739 all domains of life suggest conserved features of SMC proteins: Coiled-Coil Domain of
740 *Bacillus subtilis* SMC. *Proteins Struct. Funct. Bioinforma.* **83**, 1027–1045 (2015).
741 17. Gazi, A. D., Charova, S. N., Panopoulos, N. J. & Kokkinidis, M. Coiled-coils in type III
742 secretion systems: structural flexibility, disorder and biological implications. *Cell. Microbiol.*
743 **11**, 719–729 (2009).
744 18. Ausmees, N., Kuhn, J. R. & Jacobs-Wagner, C. The Bacterial Cytoskeleton: An Intermediate
745 Filament-Like Function in Cell Shape. *Cell* **115**, 705–713 (2003).

746 19. Liu, Y., Van Den Ent, F. & Löwe, J. Filament structure and subcellular organization of the
747 bacterial intermediate filament–like protein crescentin. *Proc. Natl. Acad. Sci.* **121**,
748 e2309984121 (2024).
749 20. Komeili, A., Vali, H., Beveridge, T. J. & Newman, D. K. Magnetosome vesicles are present
750 before magnetite formation, and MamA is required for their activation. *Proc. Natl. Acad. Sci.*
751 **101**, 3839–3844 (2004).
752 21. Grant, C. R. *et al.* Distinct gene clusters drive formation of ferrosome organelles in bacteria.
753 *Nature* **606**, 160–164 (2022).
754 22. Pi, H. *et al.* Clostridioides difficile ferrosome organelles combat nutritional immunity.
755 *Nature* **623**, 1009–1016 (2023).
756 23. Schüler, D., Uhl, R. & Bäuerlein, E. A simple light scattering method to assay magnetism in
757 *Magnetospirillum gryphiswaldense*. *FEMS Microbiol. Lett.* **132**, 139–145 (1995).
758 24. Li, J. *et al.* Crystal growth of bullet-shaped magnetite in magnetotactic bacteria of the
759 *Nitrospirae* phylum. *J. R. Soc. Interface* **12**, 20141288 (2015).
760 25. Awal, R. P. *et al.* Experimental analysis of diverse actin-like proteins from various
761 magnetotactic bacteria by functional expression in *Magnetospirillum gryphiswaldense*. *mBio*
762 **14**, e01649-23 (2023).
763 26. Pohl, A. *et al.* Decoding Biomineralization: Interaction of a Mad10-Derived Peptide with
764 Magnetite Thin Films. *Nano Lett.* **19**, 8207–8215 (2019).
765 27. Pohl, A. *et al.* Magnetite-binding proteins from the magnetotactic bacterium *Desulfamplus*
766 *magnetovallimortis* BW-1. *Nanoscale* **13**, 20396–20400 (2021).

767 28. Abreu, N. *et al.* Interplay between Two Bacterial Actin Homologs, MamK and MamK-Like,
768 Is Required for the Alignment of Magnetosome Organelles in Magnetospirillum magneticum
769 AMB-1. *J. Bacteriol.* **196**, 3111–3121 (2014).
770 29. Komeili, A., Li, Z., Newman, D. K. & Jensen, G. J. Magnetosomes Are Cell Membrane
771 Invaginations Organized by the Actin-Like Protein MamK. *Science* **311**, 242–245 (2006).
772 30. Toro-Nahuelpan, M. *et al.* Segregation of prokaryotic magnetosomes organelles is driven by
773 treadmilling of a dynamic actin-like MamK filament. *BMC Biol.* **14**, 88 (2016).
774 31. Taoka, A. *et al.* Tethered Magnets Are the Key to Magnetotaxis: Direct Observations of
775 *Magnetospirillum magneticum* AMB-1 Show that MamK Distributes Magnetosome
776 Organelles Equally to Daughter Cells. *mBio* **8**, e00679-17 (2017).
777 32. Katzmann, E., Scheffel, A., Gruska, M., Plitzko, J. M. & Schüler, D. Loss of the actin-like
778 protein MamK has pleiotropic effects on magnetosome formation and chain assembly in
779 *Magnetospirillum gryphiswaldense*. *Mol. Microbiol.* **77**, 208–224 (2010).
780 33. Fields, S. & Song, O. A novel genetic system to detect protein–protein interactions. *Nature*
781 **340**, 245–246 (1989).
782 34. Komeili, A., Vali, H., Beveridge, T. J. & Newman, D. K. Magnetosome vesicles are present
783 before magnetite formation, and MamA is required for their activation. *Proc. Natl. Acad. Sci.*
784 **101**, 3839–3844 (2004).
785 35. Scheffel, A. *et al.* An acidic protein aligns magnetosomes along a filamentous structure in
786 magnetotactic bacteria. *Nature* **440**, 110–114 (2006).
787 36. Tanaka, M., Arakaki, A. & Matsunaga, T. Identification and functional characterization of
788 liposome tubulation protein from magnetotactic bacteria. *Mol. Microbiol.* **76**, 480–488
789 (2010).

790 37. Wan, J. *et al.* A protease-mediated switch regulates the growth of magnetosome organelles in
791 Magnetospirillum magneticum. *Proc. Natl. Acad. Sci.* **119**, e2111745119 (2022).
792 38. Arakaki, A. *et al.* Comparative Subcellular Localization Analysis of Magnetosome Proteins
793 Reveals a Unique Localization Behavior of Mms6 Protein onto Magnetite Crystals. *J.*
794 *Bacteriol.* **198**, 2794–2802 (2016).
795 39. Bickley, C. D., Wan, J. & Komeili, A. Intrinsic and extrinsic determinants of conditional
796 localization of Mms6 to magnetosome organelles in *Magnetospirillum magneticum* AMB-1.
797 *J. Bacteriol.* **206**, e00008-24 (2024).
798 40. Wan, J. *et al.* McaA and McaB control the dynamic positioning of a bacterial magnetic
799 organelle. *Nat. Commun.* **13**, 5652 (2022).
800 41. Gorby, Y. A., Beveridge, T. J. & Blakemore, R. P. Characterization of the bacterial
801 magnetosome membrane. *J. Bacteriol.* **170**, 834–841 (1988).
802 42. Paulus, A. *et al.* MamF-like proteins are distant Tic20 homologs involved in organelle
803 assembly in bacteria. *Nat. Commun.* **15**, 10657 (2024).
804 43. Scheffel, A. *et al.* An acidic protein aligns magnetosomes along a filamentous structure in
805 magnetotactic bacteria. *Nature* **440**, 110–114 (2006).
806 44. Draper, O. *et al.* MamK, a bacterial actin, forms dynamic filaments in vivo that are regulated
807 by the acidic proteins MamJ and LimJ: Dynamic MamK filaments are regulated by MamJ
808 and LimJ. *Mol. Microbiol.* **82**, 342–354 (2011).
809 45. Toro-Nahuelpan, M. *et al.* MamY is a membrane-bound protein that aligns magnetosomes
810 and the motility axis of helical magnetotactic bacteria. *Nat. Microbiol.* **4**, 1978–1989 (2019).

811 46. Parks, D. H. *et al.* GTDB: an ongoing census of bacterial and archaeal diversity through a
812 phylogenetically consistent, rank normalized and complete genome-based taxonomy. *Nucleic*
813 *Acids Res.* **50**, D785–D794 (2021).
814 47. Scheffel, A. & Schüler, D. The Acidic Repetitive Domain of the Magnetospirillum
815 gryphiswaldense MamJ Protein Displays Hypervariability but Is Not Required for
816 Magnetosome Chain Assembly. *J. Bacteriol.* **189**, 6437–6446 (2007).
817 48. Chariaou, M. *et al.* Anisotropy of Bullet-Shaped Magnetite Nanoparticles in the
818 Magnetotactic Bacteria Desulfovibrio magneticus sp. Strain RS-1. *Biophys. J.* **108**, 1268–
819 1274 (2015).
820 49. Kovács, A. *et al.* Influence of crystal shape and orientation on the magnetic microstructure of
821 bullet-shaped magnetosomes synthesized by magnetotactic bacteria. *Geo-Bio Interfaces* **1**, e1
822 (2024).
823 50. Chen, I.-M. A. *et al.* The IMG/M data management and analysis system v.7: content updates
824 and new features. *Nucleic Acids Res.* **51**, D723–D732 (2023).
825 51. Katoh, K. & Standley, D. M. MAFFT multiple sequence alignment software version 7:
826 improvements in performance and usability. *Mol. Biol. Evol.* **30**, 772–780 (2013).
827 52. Guindon, S. *et al.* New algorithms and methods to estimate maximum-likelihood
828 phylogenies: assessing the performance of PhyML 3.0. *Syst. Biol.* **59**, 307–321 (2010).
829 53. Constant Systems | Multi Cycle Cell Disruptor. *Constant Systems*
830 https://constantsystems.com/products/multi-cycle-cell-disruptor/.
831 54. Ehrlich, H., Bailey, E., Wysokowski, M. & Jesionowski, T. Forced Biomineralization: A
832 Review. *Biomimetics* **6**, 46 (2021).
833